Hydrogen-rich syngas production from bi-reforming of greenhouse gases over zirconia modified Ni/MgO catalyst

Ahmad Salam Farooqi [a, b]**, Mohammad Yusuf** [a, b]**, Noor Asmawati Mohd Zabidi** [b, c]**, R. Saidur** [d, e]**, Muhammad Umair Shahid** [f]**, Bamidele Victor Ayodele** [g]**, Bawadi Abdullah** [a, b*]

[a] Chemical Engineering Department, Universiti Teknologi PETRONAS, 32610 Seri Iskandar, Malaysia.
[b] Centre of Contaminant Control and Utilization (CenCoU), Institute of Contaminant Management for Oil and Gas, Universiti Teknologi PETRONAS, 32610 Seri Iskandar, Malaysia.
[c] Fundamental and Applied Sciences Department, Universiti Teknologi PETRONAS, 32610 Seri Iskandar, Malaysia.
[d] Research Centre for Nano-Materials and Energy Technology (RCNMET), School of Engineering and Technology, Sunway University, Jalan University, 47500, Bandar Sunway, Selangor, Darul Ehsan, Malaysia.
[e] Department of Engineering, Lancaster University, Lancaster LA1 4WY, UK.
[f] Department of Materials Science and Engineering, Institute of Space Technology, Islamabad, Pakistan.
[g] Institute of Energy Policy and Research, Universiti Tenaga Nasional, Jalan IKRAM-UNITEN, 43000 Kajang, Selangor, Malaysia.

*Corresponding author: bawadi_abdullah@utp.edu.my, bawadi73@gmail.com

Abstract

Bi-reforming of methane (BRM) is gaining increasing interest due to the critical requirements to mitigate global warming and provide alternative energy resources. However, there has been a serious challenge to the scale-up of the process to commercial production due to the catalyst deactivation. In the present study, the influence of ZrO_2 modifications on the activity and stability of MgO-supported Ni catalyst in the BRM reaction was investigated. The ZrO_2-MgO mixed oxide support was prepared by co-precipitation method with variation in the ZrO_2 composition and subsequently impregnated with Ni. The characterization of the freshly prepared Ni/MgO and Ni/MgO-ZrO_2 catalysts using N_2 physisorption analysis, X-Ray Diffraction (XRD), FESEM, H_2-TPR, and CO_2-TPD techniques revealed suitable physicochemical properties for the BRM reaction. The Ni/MgO-ZrO_2 catalysts showed an improved performance in the BRM reaction in terms of activity and stability compared to the Ni/MgO at 800 °C and CH_4, H_2O, CO_2 ratio of 3:2:1, respectively. The best performance was obtained using the Ni/15%ZrO_2-MgO for the BRM with CO_2 and CH_4 conversion of 81.5% and 82.5%, respectively. The characterization of the spent Ni/MgO catalyst using Raman spectroscopy, FESEM and Transmission Electron Microscopy (TEM) analysis revealed the formation of amorphous carbon that could be responsible for its fast deactivation.

Keywords- BRM; greenhouse gases; impregnation; co-precipitation; amorphous carbon

1. Introduction

In the last few decades, huge amounts of energy have been utilized for rapid industrial development that was mainly met by fossil fuel consumption [1]. The ever-increasing use of

fossil fuels significantly contributes to the rise in the emissions of CH_4 and CO_2, which are key components of greenhouse gases. These greenhouse gases have adversely affected the environment leading to an increase in sea levels causing catastrophic floods and storms [2,3]. Converting CH_4 and CO_2 to synthetic gas can help mitigate their effects on the environment and also serve as a pathway for producing alternative clean fuel through Gas-to-Liquid (GTL) technologies. Synthesis gas (syngas), a mixture of hydrogen and carbon monoxide is used as feedstock in the production of a variety of hydrocarbons, fuels, and oxygenates through reforming processes [4,5]. In particular, steam-CO_2 reforming of methane, also termed as bi-reforming of methane (BRM) (Eq. 1) is a feasible method for producing syngas with a molar ratio of 2, which is desired feedstock for Fischer-Tropsch (F-T) synthesis. This is due to the advantage of high catalytic stability in the co-existence of CO_2 and H_2O oxidizing reactants and a flexible adjustment of H_2/CO ratios by manipulating feedstock composition. BRM is a potential replacement for other conventional reforming processes [6–8]. The BRM reaction mainly consists of steam methane reforming SMR (Eq. 2), water gas shift, WGS (Eq. 3) reaction, and dry methane reforming, DMR (Eq. 4) [9].

BRM:	$3CH_4 + 2H_2O + CO_2 \rightarrow 8H_2 + 4CO$	$(\Delta H^o_{298K} = +712 kJ/mol)$	(1)
SMR:	$CH_4 + H_2O \rightarrow CO + 3H_2$	$(\Delta H^o_{298K} = +206 \ kJ/mol)$	(2)
WGS:	$CO + H_2O \rightarrow CO_2 + H_2$	$(\Delta H^o_{298K} = -41 kJ/mol)$	(3)
DMR:	$CH_4 + CO_2 \rightarrow 2CO + 2H_2$	$(\Delta H^o_{298K} = +247 kJ/mol)$	(4)
POM:	$CH_4 + \frac{1}{2} O_2 \rightarrow CO + 2H_2$	$(\Delta H^o_{298K} = -247 \ kJ/mol)$	(5)

Although SMR produces a high molar ratio of syngas i.e., H_2/CO ratio > 3 becomes unsuited for the downstream formation of long-chain hydrocarbons via F-T synthesis [10,11]. Also, partial oxidation of methane (POM) has been investigated to produce syngas with the ideal H_2/CO ratio of approximately 2, which is preferred for F-T synthesis [12]. However, POM (Eq. 5) has been reported drawbacks such as a high exothermic reaction, difficulties in controlling the reaction owing to the formation of a hot spot, and the possibility of explosions. Nevertheless, DMR has recently attracted the interest of industrial and academic researchers because the DMR process serves not only to reduce CO_2 emissions but is found to be a promising route to convert greenhouse gases to valuable products [12,13]. The DMR process includes an associated reverse water-gas shift (RWGS) side reaction which causes a low H_2/CO ratio (i.e., < 1), making it unsuitable for F-T synthesis [14,15]. However, undesired catalyst deactivation due to carbon formation followed by metal sintering at high temperatures was found to be present in DMR [16]. As a result, a combination of these reactions (SMR and

2

DMR) generates syngas with a suitable molar ratio for the production of clean fuels by F-T synthesis.

The family of noble metals, including Pd, Pt, Ru, and Rh has exhibited remarkable activity and resistance towards the unwanted carbon formation for BRM reaction. However, the cost of these noble metal precursors is exorbitant than the other transition metal counterparts which is the main challenge associated with the adoption of BRM at an industrial scale [17,18]. Also, Ni-based catalysts are widely used in reforming processes because of their abundant availability, affordability, and comparable catalytic activity [5,19,20]. However, the major weakness of these catalysts is their affinity of coke formation and sintering at high-temperature which results in undesired deactivation of the catalyst [21]. Thus, Ni-based catalysts have gained a wide range of attention to find out how possible reduction in coke formation. This has been possible due to the utilization of suitable compositions of the catalyst as well as the optimum synthesis and modifiers, including noble and alkaline metals [22,23].

The nature of the catalyst support is crucial to develop catalysts possessing high activity and stability for BRM. In this context, an alkaline earth metal oxide such as MgO can be referred to as a good choice for support material for methane reforming based on having strong surface basicity and high thermal stability [24]. Furthermore, the selection of support material relies predominantly on the good number of oxygen available on its surface, improving CO_2 adsorption and dissociation [25]. Besides, metal oxide such as MgO or ZrO_2 has attracted huge interest as either a promoter and/or support in the BRM because they offer exceptional chemical and thermal stability and high oxygen mobility with carbon resistance [26–29]. Dębek et al. [30] and Swirk et al. [31] proved that ZrO_2 as a promoter could increase the basicity of hydrotalcite-derived Ni-Mg-Al catalysts, thereby enhancing the CO_2 adsorption which leads to the removal of carbon. Xu and coworkers showed that using nanoparticles of ZrO_2 or MgO as support material provided highly active and stable reforming reactions [28,32]. In addition, Jing and Zheng [33] found that the use of ZrO_2 as a modifier to the Ni/SiO_2 catalysts rendered better Ni dispersion which acted to improve the catalytic activity and resistance of Ni sintering.

Although utilization of MgO and ZrO_2 as support for individual catalysts has attracted significant attention in methane reforming. However, there is still a need to investigate the application of mixed oxide ZrO_2-MgO supported Ni catalysts for BRM. Thus, the primary aim of this research is to study the influence of various ZrO_2 loadings (0, 5, 10, 15, and 20 wt.%) over Ni/MgO catalyst on the catalytic performance and carbon deposition during the BRM

reaction. The freshly prepared catalysts were studied by BET, XRD, FESEM, H_2-TPR, and CO_2-TPD techniques. The BRM reaction was conducted at 800 °C and 1 atm by feeding CH_4, H_2O, CO_2 at a stoichiometric ratio of 3:2:1, respectively. Further, FESEM, Raman spectroscopy, and TEM characterization techniques were employed to analyze the spent catalysts to determine the type of carbon formed on the catalyst surface during the reaction.

2. Experimental

2.1 Formulation of catalysts

The ZrO_2-MgO mixed support (5, 10, 15, and 20 wt.% of ZrO_2) were formulated using the co-precipitation technique by utilizing the salts as precursor chemicals i.e., zirconium (IV) oxynitrate hydrate ($ZrO(NO_3)_2.xH_2O$) and magnesium nitrate hexahydrate ($Mg(NO_3)_2.6H_2O$). Stoichiometric amounts of precursors chemicals were dissolved in D.I. water followed by perpetual stirring till a clear solution was formed. Subsequently, ammonia solution (28 wt.%) as a precipitate agent was added drop wisely to keep the pH of the solution in the range of 9-9.5. The obtained mixture was constantly stirred at 80℃ until the pH value was steadied at 9.5. Then, the mixture was kept for aging overnight at ambient temperature. The resultant precipitate that has formed is washed with distilled water and filtered to remove any contaminants. After that, the resulting slurry was dried at 110℃ overnight ==before== calcination at 850℃ for 4h in static air at a heating rate of 5℃/min. The calcined supports are labeled $xZrO_2$-MgO, where x denotes the weight percent of zirconia.

The as-prepared supports were then impregnated with a Ni $(NO_3)_2.6H_2O$ solution, resulting in a final catalyst that contained approximately 10wt. % Ni metal. The mixture was then continuously stirred at 80℃ for 5 h. The excess water was evaporated by drying the sample at 110℃ for 12 h before being calcined in static air at 850℃ for 4 h [23]. Hence, a variety of different catalysts with 10 wt.% Ni amounts have been prepared as Ni/MgO, Ni/MgO-5%ZrO_2, Ni/MgO-10%ZrO_2, Ni/MgO-15%ZrO_2, and Ni/MgO-20%ZrO_2 and referred to as NM, MZ5, MZ10, MZ15, and MZ20, respectively.

2.2 Catalyst characterizations

X-ray diffraction patterns were obtained for all the calcined catalysts using Advance Bruker D8B X-ray diffractometer, USA. The Data was collected with a diffraction angle ranged from 5−90° with scan slim and step size of 1° and 0.05 °, respectively. When analyzing the powder

samples, the crystal phases present were identified by using ICDD databases as a reference for the characteristic crystal system.

The textural properties of the synthesized catalysts were determined from N_2 adsorption-desorption isotherms at -196 ℃ using a Micromeritics Tristar 3020 analyzer. Prior to the tests, the samples were outgassed at 200 ℃ for 8 h under vacuum. The Brunauer-Emmett-Teller (BET) method was used to determine the surface area in the relative pressure range (p/po) between 0.05-0.20. Further, the total pore volume was measured at a relative pressure of 0.96. The morphology of the as-prepared catalysts was studied by the FESEM instrument equipped with EDC (Zeiss Supra 55VP).

H_2-TPR experiment was carried out in a Thermo Finnigan TPDRO 1100 instrument, fitted with a thermal conductivity detector (TCD). Prior to the experiment, the catalyst samples (~ 50 mg) were pretreated under an N_2 flow at 150 ℃ for 1 h, cooling to room temperature, and then 10% H_2/N_2 (30 mL/min) was introduced. The H_2-TPR process was conducted from 40 to 850 ℃ with a heating rate of 10 ℃/min. The CO_2-TPD experiment was also performed on Thermo Finnigan TPDRO 1100 instrument. The catalyst samples (0.1 g) were pretreated at 250 ℃ with He for 30 min before the adsorption experiments. After that, the desorption process was performed from 30 to 900 ℃ with a heating rate of 10 ℃/min, in a He flow rate of 30 mL/min. The corresponding CO_2 desorption signal was measured using a TCD detector.

The Raman spectra were acquired with the use of a LabRAM spectrometer at room temperature with a 514 nm emission line from an Ar^+ laser beam. X-ray electron microscopy was performed on the freshly prepared catalysts using an XSAM800 spectrometer with Al Kα (hv = 1486.6 eV). The collected spectra were calibrated based on the binding energy of the C 1s peak (284.6 eV). High-Resolution Transmission electron microscopy (HRTEM) images were taken in a Philips Technai 20 microscope, operating with a tungsten filament working at 200 kV.

2.3 Methane bi-reforming performance test

The BRM catalytic reaction was conducted in a tubular fixed-bed reactor with dimensions (L = 4.3 cm and I.D. = 1 cm). Figure 1 describes the schematic diagram of the reactor setup in detail. A thin quartz wool layer mounted a sample of 0.1 g of each catalyst sample and retained it in the center of the reactor for constant heating throughout the reaction. The H_2 and N_2 serve as reducing and diluent gases, while CH_4 and CO_2 serve as the reacting gases. The flow rates of the reactants were monitored using mass flow controllers (Brand: Alicat), while the flow rate of vaporized water was controlled by a syringe pump (model no. NE-1010). Prior to

5

entering the fixed-bed reactor, the CH_4 and CO_2 gaseous reactants were mixed with the vaporized water after being diluted with N_2 gas (ensured the total flow rate of 60 mL min^{-1}). Before the reaction was initiated, all catalysts were reduced at 800 °C for 2 h in a flow of 60 mLmin^{-1} H_2/N_2 (1:1). After that, the reactant gas mixture was introduced into the reactor to initiate the reaction for 7 h time-on-stream. The BRM reaction was performed at 800 °C with stoichiometric feed-composition of CH_4: CO_2: H_2O = 3:1:2 under atmospheric pressure. The reaction products were analyzed by Agilent 7820 Series Gas chromatogram system fitted with flame-ionization detector (FID) and thermal conductivity detector (TCD). The unreacted steam in effluent gases was condensed and completely adsorbed by a cold trap and a drierite adsorbent bed, respectively before Gas Chromatography (GC) analysis.
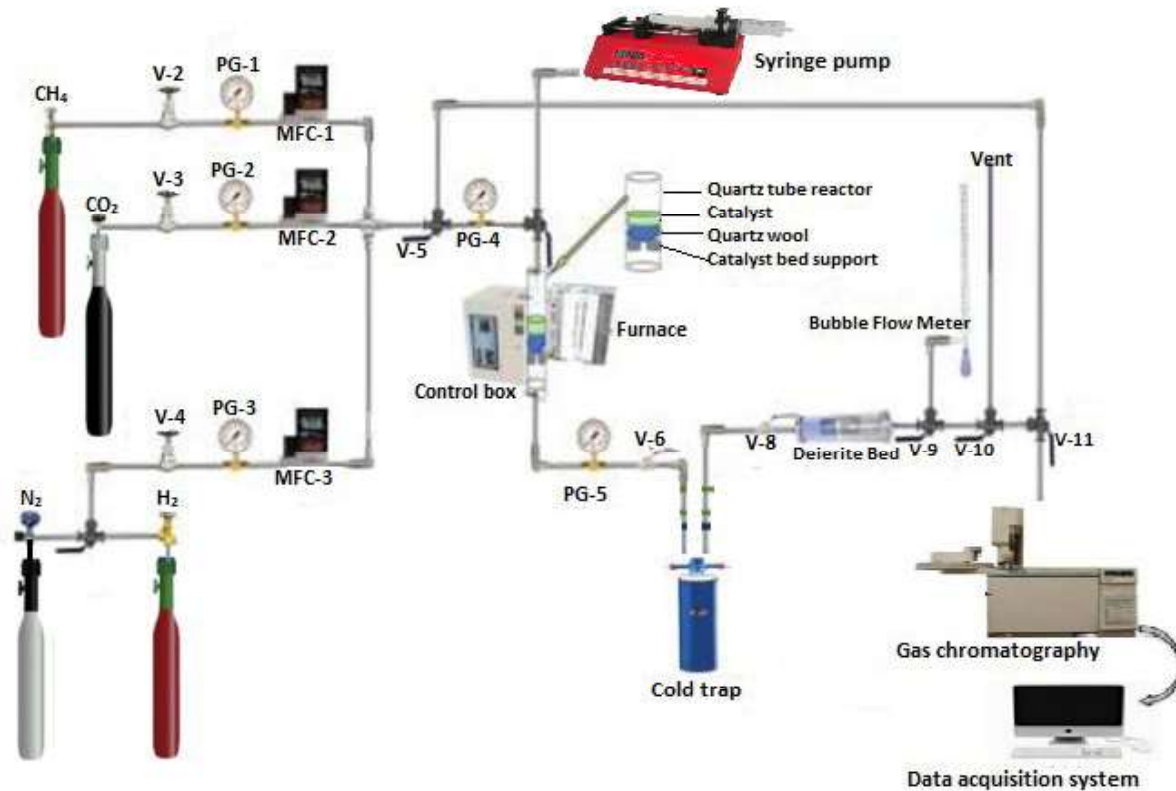
Figure 1. Schematic diagram of BRM reactor

The subsequent equations were employed to compute the conversions of CH_4 and CO_2, along with the syngas ratio (H_2/CO),

$$X_{CH4}(\%) = \frac{F_{CH4in} - F_{CH4out}}{F_{CH4in}} \times 100 \qquad (6)$$

$$X_{CO2}(\%) = \frac{F_{CO2in} - F_{CO2out}}{F_{CO2in}} \times 100 \qquad (7)$$

6

$$H_2/CO = \frac{F_{H2out}}{F_{COout}} \qquad\qquad (8)$$

Where F_{in} and F_{out} are the corresponding inlet and outlet molar flow rates (mol s^{-1})

3. Results and discussion

3.1. XRD analysis

The crystalline phases and orientation of the catalysts were determined by the XRD analysis. Different peaks have been observed, which correspond to MgO, NiO, ZrO$_2$, and Ni-Mg-Zr, as given in Figure 2. The diffraction peaks of the bulk cubic phase of MgO at 2θ= 37.0º, 42.8º, 62.3º, 74.7º, and 79.0º (ICCD file no. 01-077-2364) corresponds to the planes (111), (200), (220), (311) and (222), correspondingly. The overlapping of the XRD peaks of MgO and NiO can be attributed to the dispersion of NiO in the MgO during XRD analysis [13,34]. This occurrence was explained by Long et al. [35] as the formation of solid NiMgOx complex and the effective substitution of Mg^{2+} by Ni^{2+} during the impregnation process. In general, depending on the annealing temperature, ZrO$_2$ can take one of different crystallographic forms namely pure ZrO$_2$ which occurs in the monoclinic phase at ambient temperature, shifting to the tetragonal phase at 1170 °C; the cubic phase at temperatures near to 2370 °C and melts at 2680 °C [36]. Cubic and monoclinic phases were shown to have lower catalytic activity than tetragonal phases [37]. Therefore, the desired phase that could enhance catalytic performance is tetragonal zirconia (t-ZrO$_2$), which has both acidic and basic characteristics and is involved in numerous heterogeneous catalytic systems [38,39]. Moreover, the identified peaks of t-ZrO$_2$ appear at 2θ= 29.2º, 35.3º, 50.4º, 58.9º, 60.2º, 62.8º, and 76.1º (ICCD file no. 98-016-4862) which could be indexed to (011), (110), (012), (112), (013), (121), (022) and (023) planes. The peaks recorded at 2θ =30.4º, 35.2º, 50.7º, 60.3º, 63.2º, 74.5º, 79.1º, and 85.2º revealed the formation of a Zr-Mg-O complex (ICCD file no. 98-016-4862) having a cubic structure. The absence of metallic Ni peaks during the reduction process can be attributed to high dispersion and the strong solid interaction between MgO and NiO or MgO-ZrO$_2$ [32].
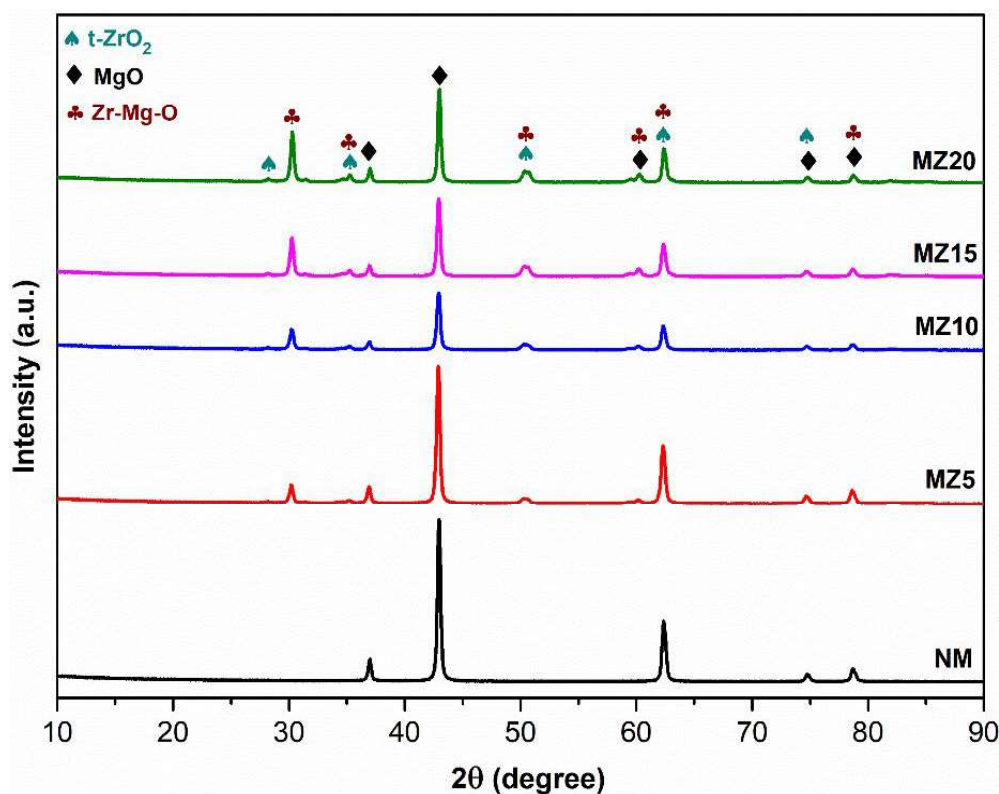
Figure 2. XRD patterns of Ni catalysts supported on MgO-ZrO$_2$

3.2.   N$_2$ physisorption analysis

The textural properties of the different catalysts prepared by varying zirconium contents are presented in Table 1. The pore size and volume of the NM catalyst were estimated as 3.11 nm and 0.15 cm^3/g, respectively, while the surface area of 34.5 m^2/g was obtained. Since the pore size of NM is greater than 2 nm, it can be inferred that the catalyst possesses mesoporous nature. However, incorporating the ZrO$_2$ as mixed oxide support reduces the surface area and pore volume of the catalysts. The existence of pore-blocking connected with the impregnation process could result in the reduction of the specific surface area, which is in accordance with the literature [40,41]. Besides, the decline in the surface area with the incorporation of ZrO$_2$ may be ascribed to high calcination temperature, nevertheless has the benefit of achieving a stable catalyst structure [42].

The crystallite size for the XRD peaks of the MgO (200) plane was estimated using the Debye-Scherrer equation. The results revealed that the size of the crystallites was related to the quantity of ZrO$_2$ in the catalysts. One viable explanation for this pattern is that residual Ni deposited on the samples' surfaces might hinder the formation of MgO crystallites. The recorded crystallite sizes were 30.64, 24.08, 22.61, 21.10, and 20.62 nm for NM, MZ5, MZ10, MZ15, and MZ20, respectively.

Table 1. Textural properties of the synthesized catalysts

Catalyst	S_{BET} (m²/g)	D_p (nm)	V_p (cm³/g)	C_s (nm)
Ni/MgO (NM)	34.5	3.11	0.15	30.64
Ni/5%ZrO$_2$-MgO (MZ5)	30.2	4.49	0.18	24.08
Ni/10%ZrO$_2$-MgO (MZ10)	28.7	4.35	0.19	22.61
Ni/15%ZrO$_2$-MgO (MZ15)	29.5	4.00	0.17	21.10
Ni/20%ZrO$_2$-MgO (MZ 20)	26.1	3.61	0.15	20.62

S_{BET}, D_p, V_p and C_s represent the BET surface area, pore size, pore volume and crystallite size respectively.

The N$_2$ adsorption-desorption curves of various catalysts (NM, MZ5, MZ10, MZ15, and MZ 20) have been shown in Figure 3(a). According to the IUPAC system, the isotherms obtained belong to the IV type, suggesting the mesoporous nature of the prepared catalysts (i.e., 2-50 nm) [43]. Furthermore, hysteresis curves are obtained and fit into a type H3 hysteresis loop class for 0.05-0.96 p/po range, confirming substantial mesoporous channels' [43]. Figure 3(b) depicts the results of the BJH pore size distribution of the various catalysts tested. The pore size distribution of formulated catalysts shows relatively constructed peak values of around 3-5 nm, which demonstrates the development of mesoporous materials [44].
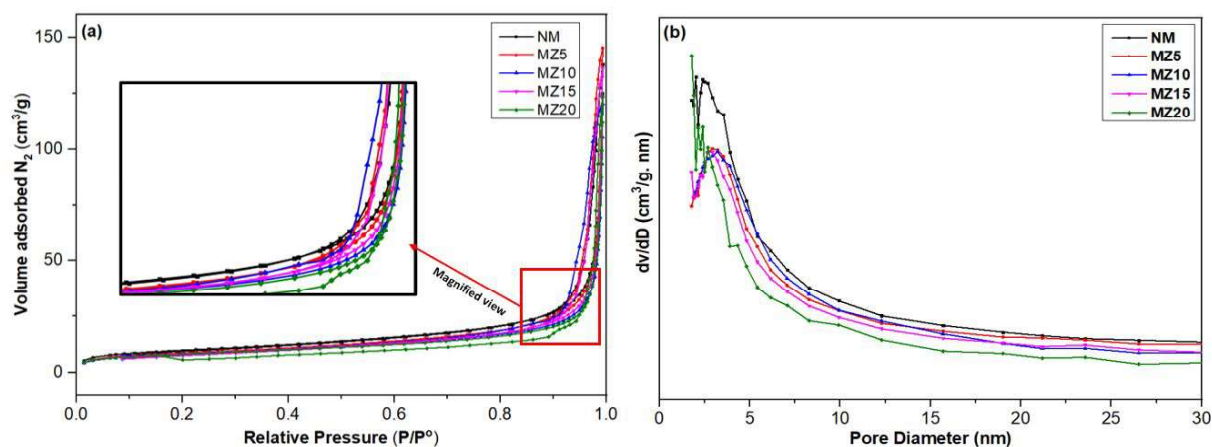

Figure 3. (a) N$_2$ adsorption-desorption isotherms and (b) BJH pore size distribution curves for different prepared catalysts

3.3.   TPR-H$_2$ analysis

Figure 4 shows the TPR profiles for the as-prepared catalysts after being calcined at 850 ℃. The TPR profile of the NM catalyst shows two distinct peaks at 506 ℃ and 682 ℃. These peaks can be attributed to the sequential reduction of NiO in interaction with the MgO support. For MZ5, there are three distinct peaks at 476 ℃, 542 ℃, and 746 ℃ [45]. The peaks at 476 ℃ and 542 ℃ could be attributed to the sequential reduction of NiO in interaction with the MgO and

ZrO$_2$ [46]. While the peak at 746 ℃ could be attributed to the reduction of NiO in interaction with ZrO$_2$-MgO. MZ10 and MZ15 have reduction peaks at 486 ℃ and 799 ℃, respectively. The peak at 486 ℃ and 799 ℃ can be attributed to NiO reduction in interaction with the MgO support and ZrO$_2$-MgO support, respectively. The distinct peaks at 221 ℃ and 481 ℃ observed for MZ20 can be attributed to the sequential reduction of NiO in weak interaction with MgO and interaction with ZrO$_2$-MgO. The various peaks observed for the catalysts show that there is an occurrence of different levels of interaction of the NiO with MgO support and, ZrO$_2$-MgO complex. The Overlap between the NiO and the reduction of the ZrO$_2$ peaks could be attributed to a strong interaction which resulted in a well-dispersed promoter and a high degree of interaction with the Ni species [47]. The NM catalyst had the lowest H$_2$ uptake, indicating that it has the fewest sites available for BRM reaction.
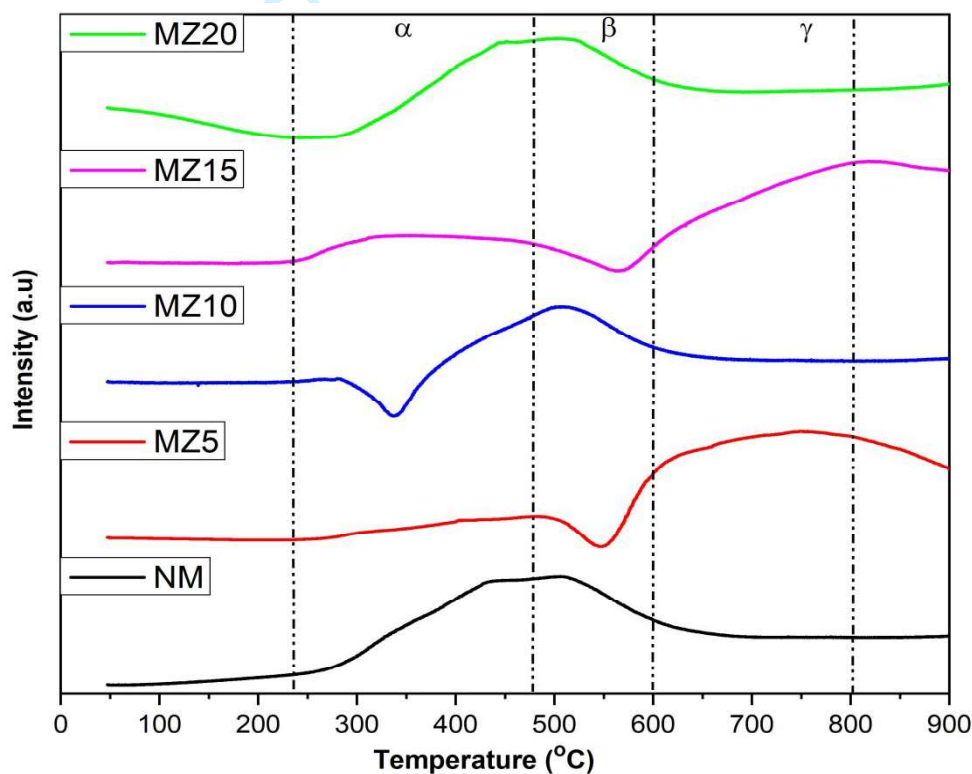

Figure 4. H$_2$-TPR profile of different synthesized catalysts

The uptakes of the H$_2$ by the reduction of NiO for each of the catalysts are depicted in Table 2. The total H$_2$ consumption of the MZ20 is higher than that of other catalysts, which could be attributed to the reduction of NiO in weak interaction with MgO and strong interaction with ZrO$_2$-MgO complex. Apart from the NM, the H$_2$ uptakes increase with an increase in ZrO$_2$ amount, which can be attributed to the stronger interaction between NiO and ZrO$_2$-MgO complex. Furthermore, the reducibility of the catalysts improved with the addition of the ZrO$_2$,

particularly those with MgO support [41]. The presence of ZrO_2 has a remarkable impact on the catalysts' redox properties by initiating oxygen mobility and modifying the Ni-support interactions.

Table 2. H_2-TPR and CO_2-TPD values for the freshly prepared catalysts

Catalyst	Peak temperature (℃)			Total H_2 consumed ($\mu mol\ gcat^{-1}$)[a]	Amount of desorbed CO_2 ($\mu mol/g$)[b]
	α	β	γ		
NM	---	506	682	254.10	152.84
MZ5	476	542	746	199.95	296.98
MZ10	---	486	---	207.73	315.96
MZ15	---	---	799	425.01	553.77
MZ20	229	481	---	572.77	223.11

[a] Determined from H_2-TPR analysis
[b] Measured by TPD-CO_2

3.4.   TPD-CO_2

The ability of a catalyst to adsorb CO_2 reveals its basicity, and more CO_2 adsorption implies a more basic catalyst and vice versa. The higher basicity of the catalyst minimizes the coke formation resulting in less deactivation of the catalyst [48]. The temperature at which CO_2 desorbs from the basic sites determines the strength of the catalyst surface basicity. In accordance with the available literature, peaks corresponding to CO_2 desorption at catalyst sites of weak and medium basicity are observed at a lower temperature (50–200°C) and intermediate temperature (200–450°C) ranges, respectively. On the other hand, the desorption peaks corresponding to the strong basic sites are observed at higher temperatures (450°C–800°C) ranges [23]. Basic groups including the weak Bronsted basic sites, Lewis acid-base sites, and Lewis basic sites coupled with oxygen anions are categorized as a weak, medium, and strong basic sites, respectively [49]. The CO_2-TPD plots of the calcined catalysts labeled as NM, MZ5, MZ10, MZ15, and MZ20 are depicted in Figure 5, with one distinct peak observed within the temperature range of 320-450℃ assigned to a medium basic site. The medium basic site formed owing to the Mg^{2+}-O^{2-} metal-oxygen pairs [50]. The CO_2 adsorption capacity of the catalyst can be ranked as follows: MZ15>MZ10>MZ20>MZ5>NM, and the amount of CO_2 desorbed is tabulated in Table 2. The property of the basic site is improved with the addition of ZrO_2, which is confirmed with a more significant proportion of CO_2 being on the catalyst's surface [51]. Furthermore, higher ZrO_2 loading, i.e., 20wt%, led to the formation of weak basic sites

11

and decreased the content of strong basic sites for MZ20 catalyst due to the acidification of catalyst, as shown in Figure 5. The CO_2 uptakes summarized in Table 2 are also an indication of the degree of basicity of the catalyst. MZ15 having the highest CO_2 uptake of 553.77 µmol/g indicates the strongest basic site. It also shows that catalysts have a varying degree of basicity.
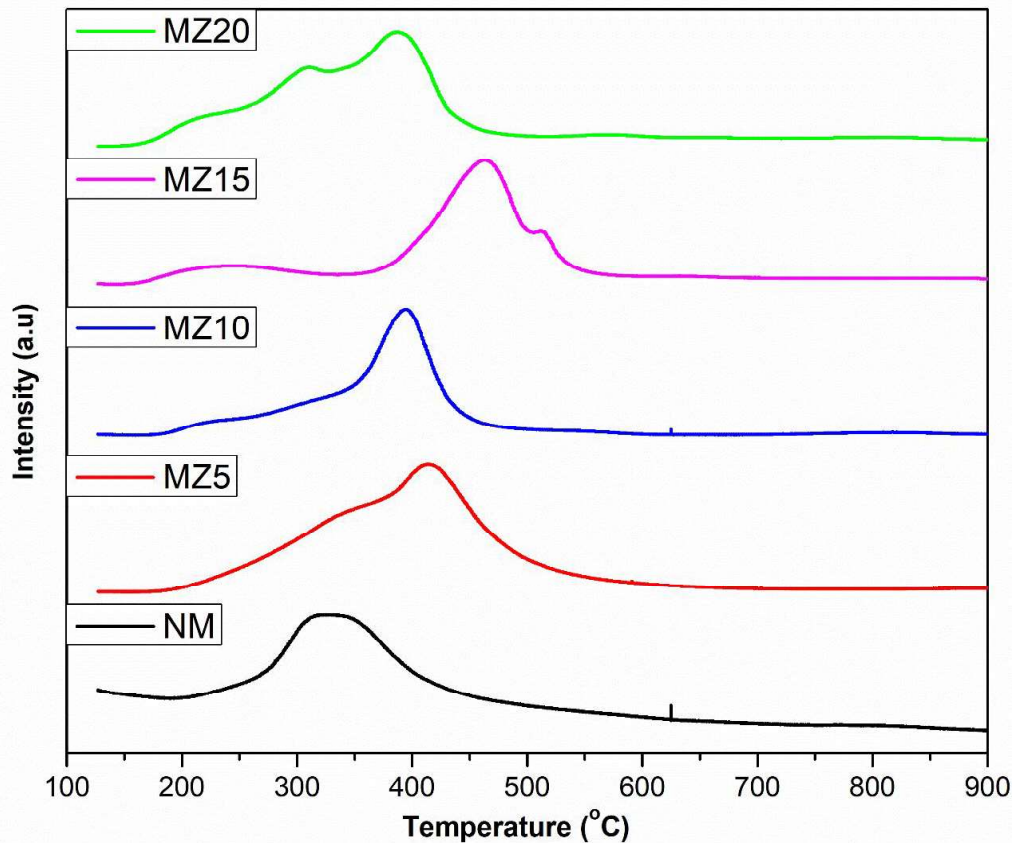

Figure 5. CO_2-TPD profile of different synthesized catalysts

3.5.   FESEM-EDX analysis

The FESEM images of freshly prepared catalysts have been examined at a magnification of 200 nm, as shown in Figure 6. The images show an apparent change when zirconia is added to the samples. The NM catalyst structure comprises clustered particles that are compact and have a low porosity of the remaining pores compared to other catalysts. With the addition of zirconia, the crystals are small-grained with defined shape and size. The ZrO_2 contains dispersive characteristics, which reduce particle size and creates bulk oxygen vacancies. Besides, the particles in these catalysts are aggregated to generate pores and develop porous texture, as shown in Figure 6. Thus, the structure of all the catalysts seems like that staghorn-coral-like morphology. Interestingly, the generation of the irregular spherical Ni nanoparticles over the

12

surface of the MgO-ZrO$_2$ could be attributed to the proper dispersion of the Ni nanoparticles, which can be observed in Figure 6(b–e).
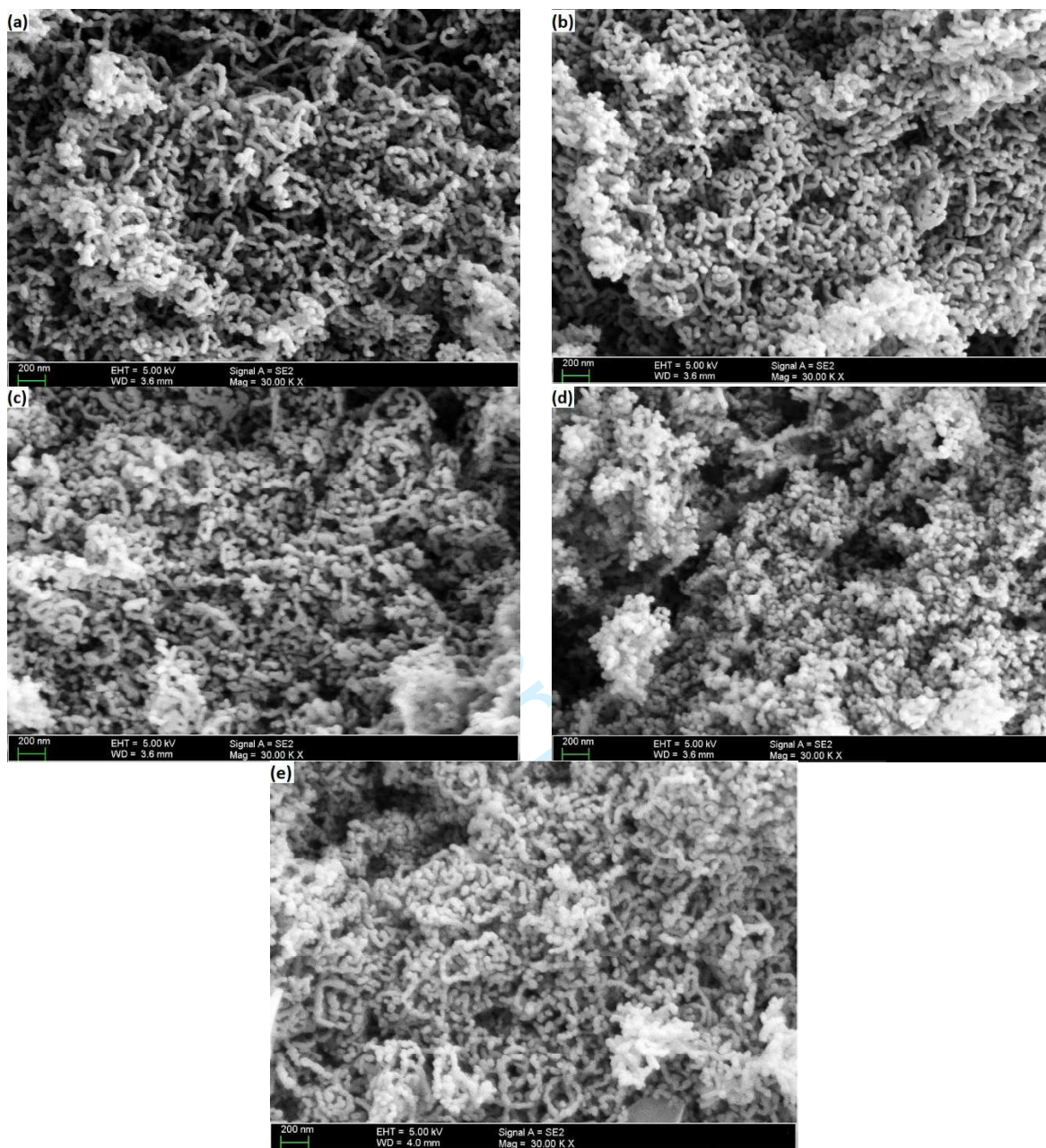

Figure 6. FESEM images of prepared catalysts: (a) NM, (b) MZ5, (c) MZ10, (d) MZ15 and (e) MZ20

The Energy Dispersive X-Ray (EDX) analysis of the synthesized nanocatalysts has been analyzed for determining the elemental composition. Figure 7(a-e) shows the EDX spectra, which show the actual loading of nickel catalyst supported on MgO-ZrO$_2$ support. The actual Ni loading of 9.3%, 10.5%, 10.3%, 11.0%, and 10.5% was obtained for NM, MZ5, MZ10, MZ15, and MZ20 respectively, which agrees with the stipulated 10wt% formulation employed in the current work.
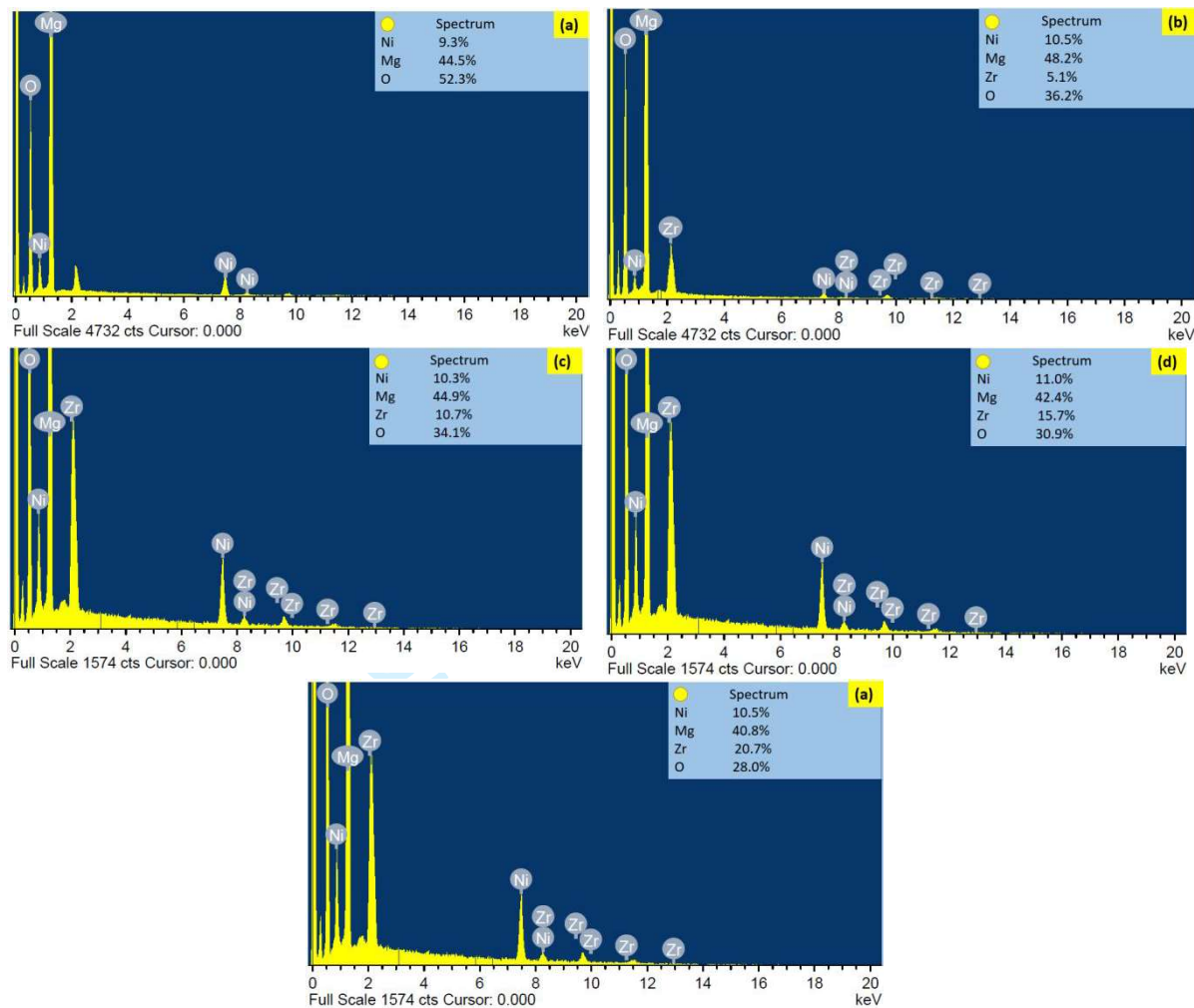
Figure 7. EDX spectra showing the elemental composition of fresh catalysts: (a) NM, (b) MZ5, (c) MZ10, (d) MZ15 and (e) MZ20

3.6.   Catalytic performance evaluation

The catalytic activity and stability of the synthesized catalysts (i.e., NM, MZ5, MZ10, MZ15, and MZ20) were tested in view of BRM reaction in a fixed bed tubular reactor. The catalytic performance during the reaction provided the significance of the catalyst towards the efficient BRM process. The BRM reaction was carried out for 7h time-on-stream at 800 ℃ under atmospheric pressure and GHSV of 36000 cm^3 g_{cat}^{-1} h^{-1}. The conversion profiles of CH_4 and CO_2 of all the samples tested at 800 ℃ against reaction time-on-stream for BRM reaction are shown in Figure 8(a-b). The conversions of CH_4, CO_2, and H_2/CO were estimated from Eqns. (6-8). With all samples, the conversion of reactants suffered a slight fall in the course of 7 h of reaction. Whereas in the case of the Ni-catalysts supported on ZrO2-MgO mixed oxide, higher conversions were observed than the Ni-catalysts supported on pure MgO (NM). Further, the NM catalyst generally showed a lesser conversion, dropping from 63.5% to 60% and 63% to 59.6%, representing CH_4 and CO_2, respectively. This revealed the constructive role of ZrO_2 on

14

the catalytic performance in terms of activity and stability of the catalysts. However, in case of the other catalysts, the conversion of CH_4 declined from 71.2% to 69.5% for MZ5, 79.5% to 75.6% for MZ10, 83.1% to 82.5% for MZ15, and 82% to 76.5% for MZ20, respectively. A similar decline occurred in the CO_2 conversion with initial conversion of 70.5%, 74.9%, 82.4%, and 78.7% to final conversions of 66.5%, 72.5%, 81.5%, and 73.7% representing MZ5, MZ10, MZ15, and MZ20, respectively. However, it is noteworthy that the MZ15 catalyst behaved far more consistently than the other catalysts during the 7 h BRM reaction test. However, a modest drop in conversion for both CH_4 and CO_2 occurs in the case of the MZ15 catalyst, which portrays it as the best performing catalyst as compared to the other prepared catalysts. Furthermore, as shown in Figure 8(c), it can be seen that the MZ15 catalyst was upheld to be the most stable catalyst as well since the H_2/CO ratio varied from 1.6 to 1.7 throughout the reaction. Table 3 summarizes the catalytic performance of different catalysts tested in BRM, and it is clearly shown that $10\%Ni/MgO-ZrO_2$ demonstrated comparable catalytic activity ($XCH_4 = 82.5$, $XCO_2 = 81.5$) at 1073 K after 7 h of reaction.
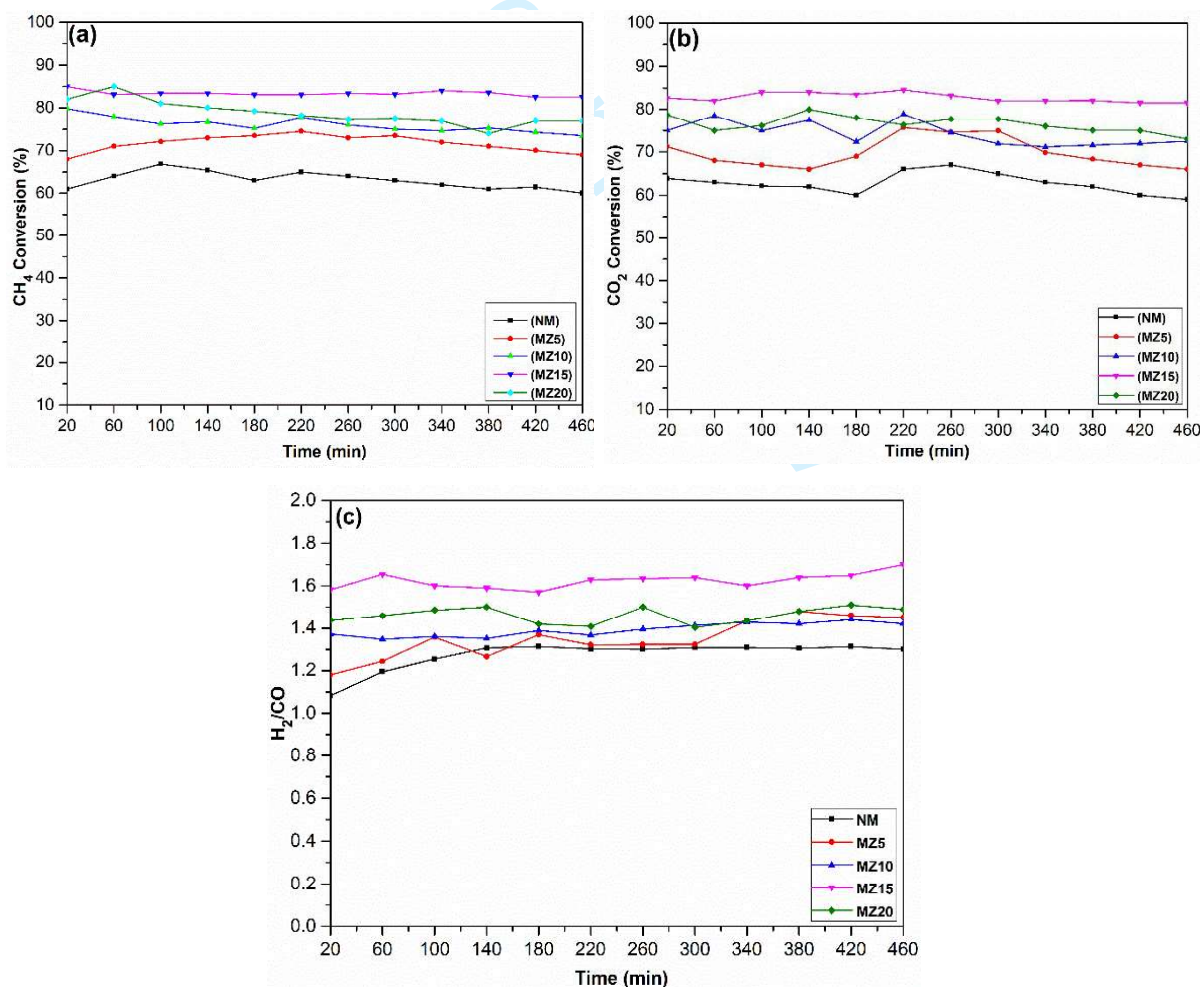

Figure 8. Performance evaluation of different synthesized catalysts in BRM reaction (a) CH_4 conversion; (b) CO_2 conversion; (c) syngas ratio

15

In the case of all the catalysts, CH_4 conversion was found higher than that of CO_2. It is well known that the water gas shift reaction (i.e., $CO + H_2O \rightarrow CO_2 + H_2$) can shift the reaction equilibrium of CO_2 reforming of CH_4, which proves responsible for achieving higher conversion of CH_4 through steam reforming. This is different from the outcomes when methane was reformed dry in the presence of CO_2, which usually follows a higher conversion of CO_2 due to the occurrence of reverse water-gas shift reaction [52].

Table 3. Summary of the catalytic performance of catalysts for BRM

Catalysts	Operating parameters					Catalytic performance			Ref
	T(℃)	P (bar)	F.R[a]	GHSV[b] (mL gcat^{-1} h^{-1})	TOS[c] (h)	XCH$_4$ (%)	XCO$_2$ (%)	H$_2$/CO[d]	
10%Ni-MgO-ZrO$_2$	800	1	3:1:2	36,000	20	82.5	81.5	1.70	This study
10%Ni/MgO	830	7	3:1.2:2.4	60,000	320	71	72	1.99	[53]
15%Ni/Ce$_{0.2}$Zr$_{0.8}$O$_2$	800	1	3:1.2:2.4	265,000	20	62	48	---	[54]
15%Ni/ZrO$_2$	800	1	3:1.2:2.4	265,000	20	70	---	---	[55]
10%Ni/MgO-Al$_2$O$_3$	800	1	3:1:2	30,000	50	94	77	2.8	[8]
5%Co/Al$_2$O$_3$-ZrO$_2$	700	1	3:3:0.6	1000	---	---	---	1.42	[56]
30%Ni/Mo-carbide	950	1	3:1.5:0.75	---	---	10	15	1.0	[57]
4%Ru/ZrO$_2$-La$_2$O$_3$	500	1	3:3:0.3	25,000	10	20	17	0.90	[58]
10%Ni/SBA-15	850	1	3:1.5:2.25	27,000	120	86	50	1.74	[18]
15%Ni/SiO$_2$	750	1	3:1.5:3	160,000	24	40	22	1.8	[59]
1.5%Pt/Ce$_{0.18}$Zr$_{0.82}$O$_2$	800	1	1:0.5:0.5	12,000	22	25	44	0.69	[60]
30%Ni/La$_2$O$_3$-NiO$_3$	650	1	3:3:1.5	70,000	20	40	31	1.44	[5]

[a] F.R is the molar ratio of the reactants (CH_4:CO_2:H_2O)

[b] GHSV stands for gas hourly space velocity (mL gcat^{-1} h^{-1})

[c] TOS stands for time on stream (h)

[d] H_2/CO is the molar ratio (mol/mol) in the products stream.

3.7. Stability test

The stability test for the MZ15 catalyst in the BRM was conducted for 20h time-on-stream at similar reaction conditions and feed rate as previously elucidated in section 3.6. The catalyst assisted in gaining an elevated conversion rate and exceptional stability throughout the reaction. There was an insignificant decrease in the conversions for CH_4 and CO_2 from 85% to 78.7% and 82.6% to 77.1%, respectively, as seen in Figure 9. Moreover, even after 20h of BRM reaction, the H_2/CO ratio in the syngas was also acceptable since it fluctuated between 1.65 and 1.55. The excellent stability of the MZ15 catalyst can be associated with several different factors that were noticed during its post-BRM reaction characterization. According to

16

post characterization study results, factors such as reducibility, increased number of active metal sites, and nature of carbon formed all prevented coke formation.
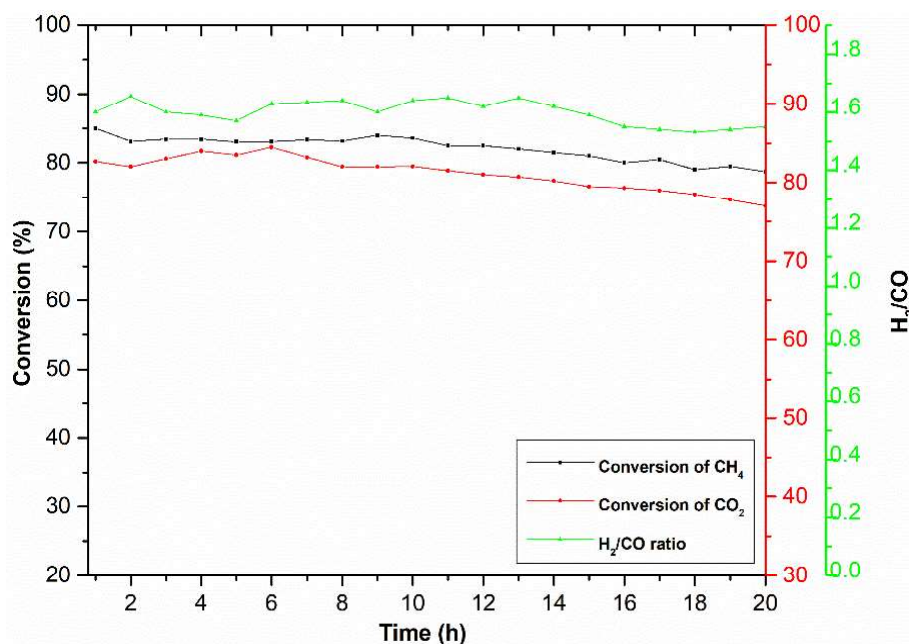

Figure 9. Long term stability test of MZ15 catalyst for 20h of BRM reaction

3.8. HRTEM of optimum catalyst

In order to examine the crystallographic structure of the NiO particles on the MgO-ZrO$_2$ support at the atomic scale, the fresh MZ15 catalyst was analyzed by the HRTEM technique as shown in Figure 10. It can be seen from the HRTEM micrographs that NiO nanoparticles with different particle sizes were located outside the pore channels of the support. Three different sized particles can be seen, the supported NiO particles which are smaller in size while, the other two-particle belong to support i.e., MgO and ZrO$_2$. It can be inferred that the NiO particles are well impregnated on the surface of the support. The support MgO is relatively large while ZrO$_2$ is between MgO and NiO. The observed particle sizes are in agreement with the crystallite size as measured by XRD. The MgO particles are grown in a rod-like structure, typically the average length is about 100 to 150 nm and diameter 50 nm. Moreover, the morphology of ZrO$_2$ particles is more or less like NiO with a relatively large size between 60 to 80 nm. The particle size distribution shows that particles lie between 20 to 140 nm. The frequency of NiO seems higher even it is only 10%, it is because support is in the background and steeped with NiO; therefore, difficult to record.
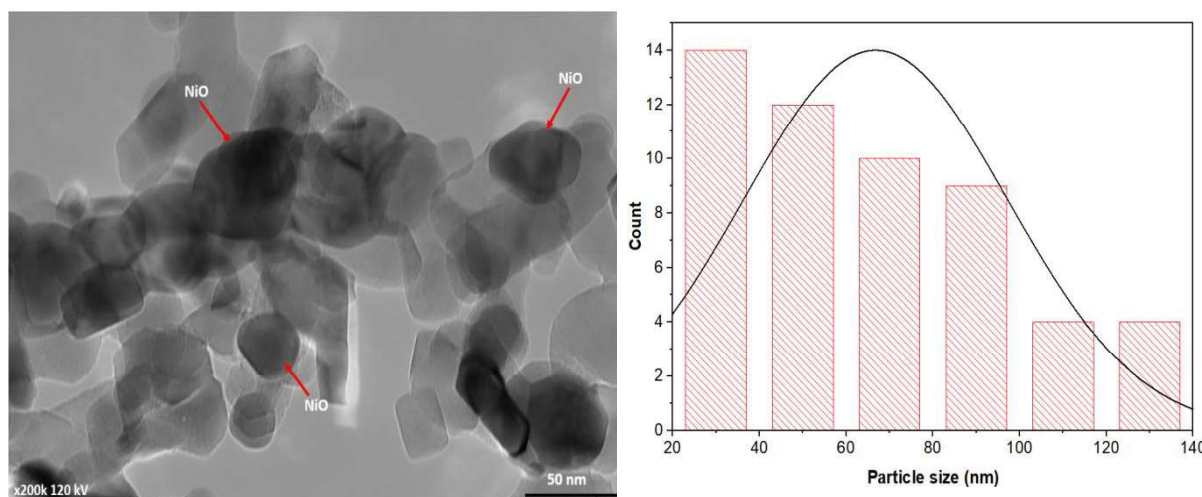
Figure 10. HRTEM image and particle size distribution of fresh MZ15 catalyst

3.9.   X-ray photoelectron spectroscopy (XPS)

Figure 11 depicts the core level high-resolution XPS analysis showing the elemental compositions and changes in the chemical states at the MZ15 catalyst surface prior to the activity test in the bi-reforming reaction. The XPS high-resolution spectra revealed the presence of distinct peaks that can be attributed to various oxidation states of elemental components. The chemical states of the various elemental components present in the MZ15 catalyst can be identified between 1320 and 0 eV. The binding energies of the distinct peaks are identified around 1306 eV, 186 eV, 880 eV and 533 eV which can be attributed to the chemical states of Mg 1s, Zr 3d, Ni 2p, and O 1s. The core XPS spectra showing the Mg 1s in Figure 11 (a) revealed the formation of MgO indicated by the binding energy at 1307 eV which is consistent with that reported by Yao et al. [61]. The two smaller peaks at binding energies of 1307.5 eV and 1304.5 eV can be attributed to the formation of other complexes of MgO such as MgO-ZrO_2. The Zr 3d identified by the high-resolution core-level XPS spectra in Figure 11 (b) also indicates a distinct peak at 185 eV which can be attributed to the formation of ZrO_2. While the two satellite peaks at 190 eV and 188 eV can be ascribed to the formation of the ZrO_2 complex such as MgO-ZrO_2. This represents the formation of mixed oxides as reported by Pawlak et al. [62].

The presence of Ni 2p at a binding energy of 855 eV also reflect two satellite peaks which can be identified at 875 eV and 865 eV and attributed to the formation of NiO (Figure 11(c)). This observation is consistent with that reported by Lv et al. [63]. Figure 11 (d) depicts the high-resolution XPS spectrum of O 1s. The O 1s has two distinct peaks at a binding energy of 533 eV and 537 eV, indicating there is the co-existence of two distinguishable chemical states of
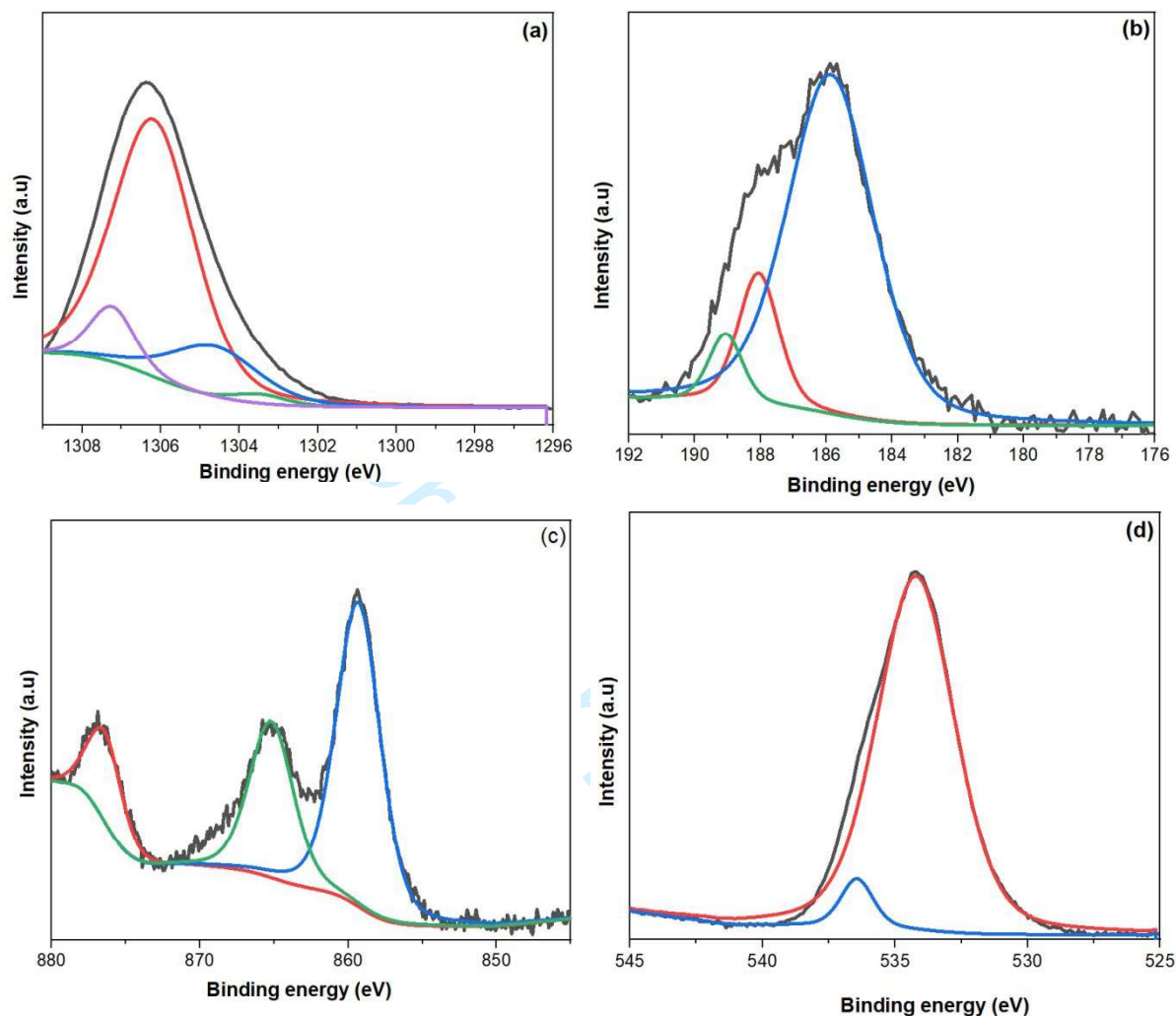
Figure 11: Core level XPS spectra for (a) Mg 1s (b) Zr 3d (c) Ni 2p (d) O 1s of the MZ15 catalyst

3.10 Post reaction characterization

3.10.1. FESEM

The FESEM images of the spent catalyst (NM) and best performing catalyst (MZ15) were investigated for carbon deposition. The FESEM images presented in Figure 12(a-b) showed that the NM catalyst formed carbon in the form of plates or sheets type. Since this encompasses the active sites of catalyst, that has a negative influence on catalytic activity [65,66]. Raman analysis substantiates that amorphous carbon or highly disordered graphitic carbon is present in this spent catalyst (NM). On the contrary, for the spent MZ15 catalyst, the carbon formed after the BRM reaction is a comparatively small amount and of different nature. Figure 12(c-

d) shows that a filamentous carbon that contains a crystalline nanotubes-like structure is being deposited on the catalyst. This is in accordance with that described in the literature [67,68]. Moreover, nanotube-like morphology presents a better surface area as compared to sheet type, which provided fast channels for gas movement during catalytic conversion reactions. On the contrary, in the case of sheet-type deposits, its poor surface area and pore size hindered the gas flow and, therefore, deteriorated the catalytic performance.
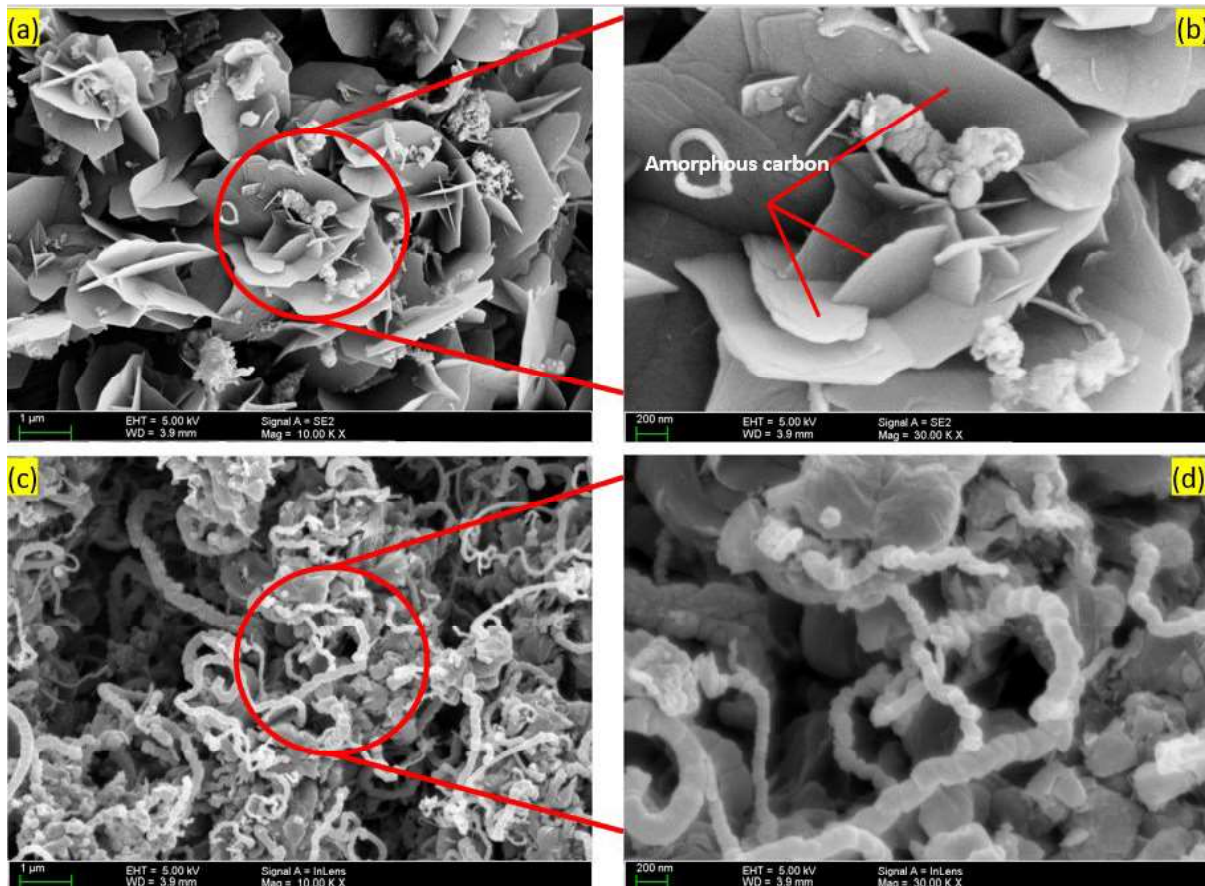
Figure 12. FESEM images of the spent catalyst; (a-b) NM catalyst; (c-d) MZ15 catalyst after 7h of BRM reaction at 800 °C.

3.10.2. RAMAN analysis

Raman spectroscopy is employed to investigate the carbon deposited on the spent catalyst. The nature of the carbon deposited on the catalyst's surface can give insight into the early deactivation of the catalysts. Figure 13 shows the Raman spectra of NM and MZ15 spent catalysts. There are mainly three peaks present in the MZ15 Raman spectrum, namely, D, G and 2D. The D peak is the breathing mode of sp^2 carbon atoms, representing the degree of intensity of defects present on graphene, CNT planes, or graphitization. The G peak indicates the E2g phonon dispersion at the Brillouin zone center; its intensity and sharpness are the

20

measures of graphitization of carbon structure. While the 2D peak is sensitive to the structure of adjacent layers of graphene and CNTs [68]. The magnitude of defects or graphitization in graphene or CNTs can be accomplished by computing the relative intensity ratio of D peak to G peak (ID/IG).

The lower the ID/IG ratio, the higher the graphitization and lower defects. The ID/IG ratio for both NM and MZ15 catalysts is given in Figure 13, and it shows that for MZ15, the ratio is much lower than NM catalyst. Therefore, a better graphitic structure can be expected in the carbon deposits of the MZ15 catalyst. In addition, the broadening in the peaks of each spectrum indicates the amorphous carbon. Moreover, a 2D peak is absent in the NM catalyst deposits that are attributed to the poor crystallinity of carbon structure. Therefore, deposits of poor crystalline or amorphous carbon in NM catalyst cause the early deactivation of the catalyst as observed in catalytic performance. On the other hand, the MZ15 catalyst produced better crystalline graphitic carbon, which leads to enhanced catalytic performance.
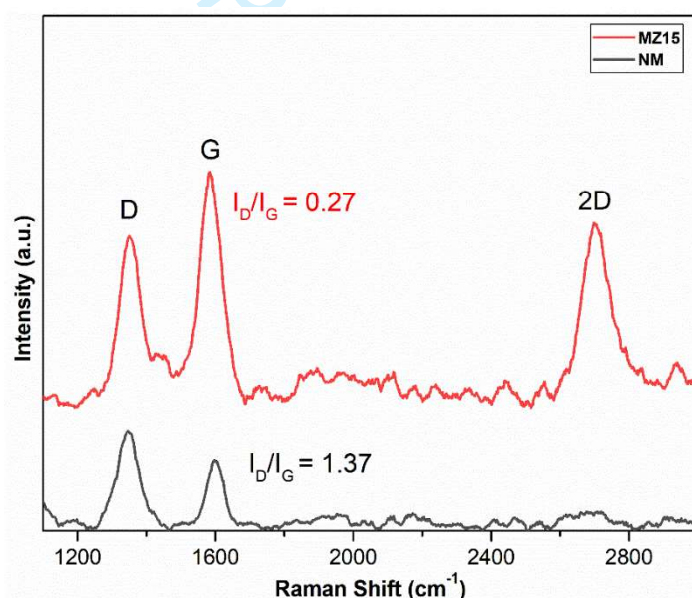

Figure 13. Raman analysis of spent (NM and MZ15) catalyst after 7h of BRM reaction at $800\ °C$.

3.10.3 HRTEM

The HRTEM images as shown in Figure 14 of spent catalysts (NM and MZ15) were taken to understand further the nature of carbon accumulated on the catalysts. Figure 14(a) shows the HRTEM image of the spent catalyst (NM) depicts that carbon nanosheets and filamentous type carbon have been formed for NM catalyst. In the case of MZ15 catalyst, Figure 14(b) shows that only filamentous carbon is formed. These results are substantiated with the findings of the FESEM study of the spent catalyst. This is because amorphous carbon nanosheets (as

21

confirmed by Raman study) covered the surface of NM catalyst and prevent reactants from coming into direct contact with the catalyst active sites. The presence of this form of carbon deposition confirms that the catalyst has a low activity [32]. On the other hand, the MZ15 catalyst generates a filamentous carbon-containing carbon nanotube (CNT) which improves the activity and stability of the catalyst. These results are in agreement with the FESEM results of the spent catalyst.
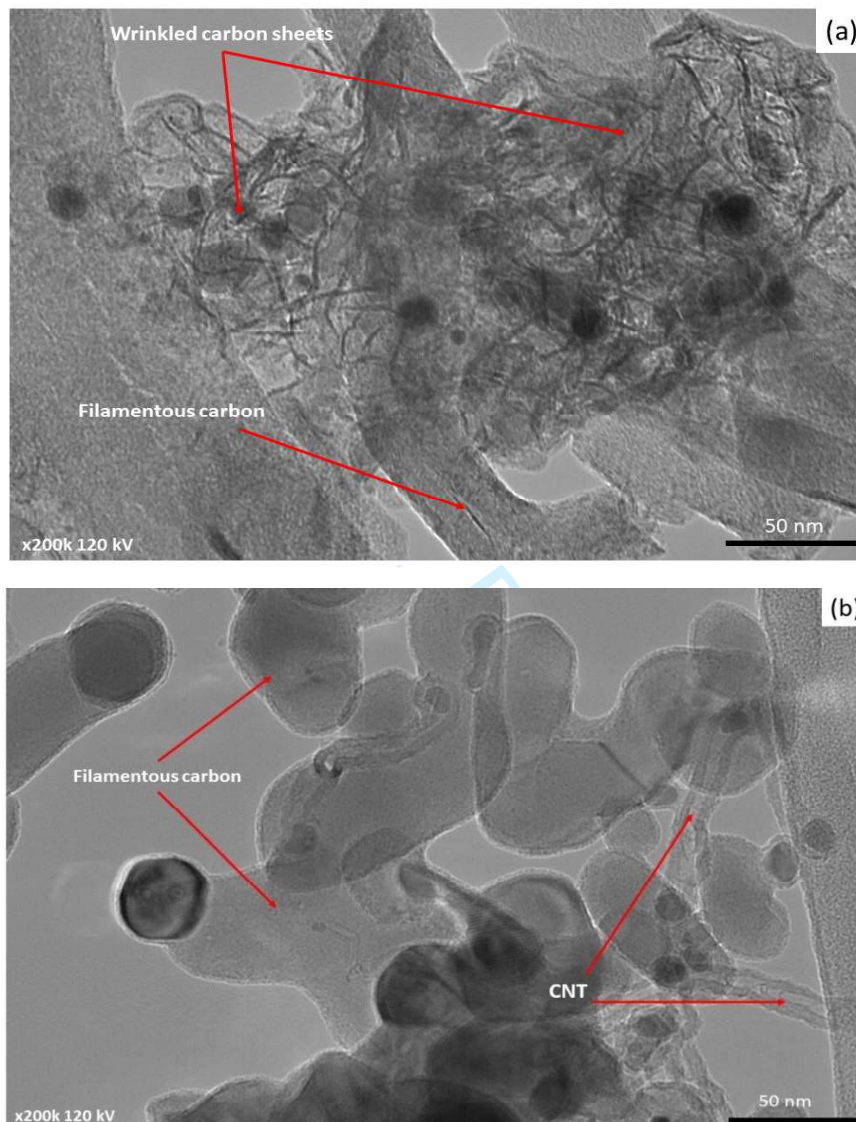

Figure 14. TEM study of spent (NM and MZ15) catalysts after BRM reaction.

4. Conclusion

This work successfully synthesized a series of Ni/xZrO$_2$-MgO (x = 0, 5, 10, 15, 20 wt.%) catalysts with 10% wt. Ni loading. The catalysts were characterized to study their textural and structural characteristics, morphology, and reducibility. The catalytic performance evaluation of the prepared catalysts was tested in the BRM reaction. The XRD results revealed the

existence of a tetragonal phase of ZrO_2, which is active in the heterogeneous catalytic system, especially in the present work for bi-reforming of methane. Besides that, the H_2-TPR data revealed that the addition of ZrO_2 acted to enrich the degree of reduction, indicating the availability of more active sites for the BRM reaction to take place. It has been found that MZ15 catalyst displayed the highest activity and stability, which resulted in satisfactorily CO_2 and CH_4 conversion rates of 81.5% and 82.5% respectively at 800 ℃. The generation of amorphous carbon nanosheets for NM catalyst and filamentous carbon for MZ15 catalyst was confirmed by FESEM, TEM, and Raman studies, respectively. The amorphous carbon-nanosheets obscured the active sites of the NM catalyst, resulting in the reduction in the activity of the catalyst. On the other hand, the MZ15 catalyst remained active as a result of the formation of CNTs.

Acknowledgments

References

[1]   Bhattacharya M, Paramati SR, Ozturk I, Bhattacharya S. The effect of renewable energy consumption on economic growth: Evidence from top 38 countries. Appl Energy 2016;162:733–41.

[2]   Manabe S. Role of greenhouse gas in climate change**. Tellus, Ser A Dyn Meteorol Oceanogr 2019;71:1–13.

[3]   Mondal MK, Balsora HK, Varshney P. Progress and trends in CO_2 capture/separation technologies: A review. Energy 2012;46:431–41.

[4]   Farooqi AS, Al-Swai BM, Ruslan FH, Mohd Zabidi NA, Saidur R, Syed Muhammad SAF. Catalytic conversion of greenhouse gases (CO_2 and CH_4) to syngas over Ni-based catalyst: Effects of Ce-La promoters. Arab J Chem 2020;13:5740–9.

[5]   Yang E hyeok, Noh YS, Hong GH, Moon DJ. Combined steam and CO_2 reforming of methane over La1-xSrxNiO3 perovskite oxides. Catal Today 2018;299:242–50.

[6]   Roh H-S, Koo KY, Jeong JH, Seo YT, Seo DJ, Seo Y-S. Combined reforming of methane over supported Ni catalysts. Catal Letters 2007;117:85–90.

[7]   Park D, Moon DJ, Kim T. Steam-CO_2 reforming of methane on Ni/γ-Al_2O_3-deposited metallic foam catalyst for GTL-FPSO process. Fuel Process Technol 2013;112:28–34.

[8]   Kang KM, Shim IW, Kwak HY. Mixed and autothermal reforming of methane with supported Ni catalysts with a core/shell structure. Fuel Process Technol 2012;93:105–14.

[9]   Lee YJ, Hong S-I, Moon DJ. Studies on the steam and CO_2 reforming of methane for GTL-FPSO applications. Catal Today 2011;174:31–6.

[10]   Singh S, Bahari MB, Abdullah B, Phuong PTT, Truong QD, Vo DVN, et al. Bi-reforming of

methane on Ni/SBA-15 catalyst for syngas production: Influence of feed composition. Int J Hydrogen Energy 2018;43:17230–43.

[11]   Usman M, Wan Daud WMA, Abbas HF. Dry reforming of methane: Influence of process parameters - A review. Renew Sustain Energy Rev 2015;45:710–44.

[12]   Christian Enger B, Lødeng R, Holmen A. A review of catalytic partial oxidation of methane to synthesis gas with emphasis on reaction mechanisms over transition metal catalysts. Appl Catal A Gen 2008;346:1–27.

[13]   Yusuf M, Farooqi AS, Al-Kahtani AA, Ubaidullah M, Alam MA, Keong LK. Syngas production from greenhouse gases using Ni–W bimetallic catalyst via dry methane reforming: Effect of W addition. Int J Hydrogen Energy 2021;46:27044–61.

[14]   Shamsuddin MR, Mansir N, Anuar A, Saiman MI, Marliza TS, Yarmo MA, et al. Insight into CO_2 reforming of CH_4 via NiO/dolomite catalysts for production of H_2 rich syngas. Int J Energy Res 2021.

[15]   Yusuf M, Farooqi AS, Keong LK, Hellgardt K, Abdullah B. Contemporary trends in composite Ni-based catalysts for CO_2 reforming of methane. Chem Eng Sci 2021;229:116072.

[16]   Abdullah B, Abd Ghani NA, Vo DVN. Recent advances in dry reforming of methane over Ni-based catalysts. J Clean Prod 2017;162:170–85.

[17]   Hossain MA, Ayodele B V, Ong HR, Mustapa SI, Cheng CK, Khan MR. Thermo-catalytic conversion of greenhouse gases (CO_2 and CH_4) to CO-rich hydrogen by CeO_2 modified calcium iron oxide supported nickel catalyst. Int J Energy Res 2020;44:6325–37.

[18]   Huang B, Li X, Ji S, Lang B, Habimana F, Li C. Effect of MgO promoter on Ni-based SBA-15 catalysts for combined steam and carbon dioxide reforming of methane. J Nat Gas Chem 2008;17:225–31.

[19]   Farooqi AS, Yusuf M, Mohd Zabidi NA, Saidur R, Sanaullah K, Farooqi AS. A comprehensive review on improving the production of rich-hydrogen via combined steam and CO_2 reforming of methane over Ni-based catalysts. Int J Hydrogen Energy 2021.

[20]   Ayodele BV, Mustapa SI, Kanthasamy R, Zwawi M, Cheng CK. Modeling the prediction of hydrogen production by co-gasification of plastic and rubber wastes using machine learning algorithms. Int J Energy Res 2021;45:9580–94.

[21]   Löfberg A, Guerrero-Caballero J, Kane T, Rubbens A, Jalowiecki-Duhamel L. Ni/CeO_2 based catalysts as oxygen vectors for the chemical looping dry reforming of methane for syngas production. Appl Catal B Environ 2017;212:159–74.

[22]   Rahbar Shamskar F, Meshkani F, Rezaei M. Preparation and characterization of ultrasound-assisted co-precipitated nanocrystalline La-, Ce-, Zr -promoted Ni-Al_2O_3 catalysts for dry reforming reaction. J CO_2 Util 2017;22:124–34.

[23]   Usman M, Wan Daud WMA. An investigation on the influence of catalyst composition, calcination and reduction temperatures on Ni/MgO catalyst for dry reforming of methane. RSC Adv 2016;6:91603–16.

[24]   Zanganeh R, Rezaei M, Zamaniyan A. Dry reforming of methane to synthesis gas on NiO–MgO nanocrystalline solid solution catalysts. Int J Hydrogen Energy 2013;38:3012–8.

[25]   Omoregbe O, Danh HT, Abidin SZ, Setiabudi HD, Abdullah B, Vu KB, et al. Influence of Lanthanide Promoters on Ni/SBA-15 Catalysts for Syngas Production by Methane Dry Reforming. Procedia Eng 2016;148:1388–95.

[26]   Li W, Zhao Z, Ren P, Wang G. Effect of molybdenum carbide concentration on the Ni/ZrO_2 catalysts for steam-CO_2 bi-reforming of methane. RSC Adv 2015;5:100865–72.

24

[27]　Zhao Z, Ren P, Li W, Miao B. Effect of mineralizers for preparing ZrO_2 support on the supported Ni catalyst for steam-CO_2 bi-reforming of methane. Int J Hydrogen Energy 2017;42:6598–609.

[28]　Zhang QH, Li Y, Xu BQ. Reforming of methane and coalbed methane over nanocomposite Ni/ZrO_2 catalyst. Catal Today 2004;98:601–5.

[29]　Rahemi N, Haghighi M, Babaluo AA, Fallah Jafari M. Syngas production via CO_2 reforming of methane over plasma assisted synthesized Ni-Co/Al_2O_3-ZrO_2 nanocatalysts with different Ni-loadings. Int J Energy Res 2014;38:765–79.

[30]　Dębek R, Galvez ME, Launay F, Motak M, Grzybek T, Da Costa P. Low temperature dry methane reforming over Ce, Zr and CeZr promoted Ni–Mg–Al hydrotalcite-derived catalysts. Int J Hydrogen Energy 2016;41:11616–23.

[31]　Świrk K, Rønning M, Motak M, Grzybek T, Da Costa P. Synthesis strategies of Zr- and Y-promoted mixed oxides derived from double-layered hydroxides for syngas production via dry reforming of methane. Int J Hydrogen Energy 2021;46:12128–44.

[32]　Al-Swai BM, Osman N, Alnarabiji MS, Adesina AA, Abdullah B. Syngas Production via Methane Dry Reforming over Ceria-Magnesia Mixed Oxide-Supported Nickel Catalysts. Ind Eng Chem Res 2019;58:539–52.

[33]　Wang Y, Zhao Q, Wang Y, Hu C, Da Costa P. One-Step Synthesis of Highly Active and Stable Ni–ZrOx for Dry Reforming of Methane. Ind Eng Chem Res 2020;59:11441–52.

[34]　Al-Fatesh AS, Fakeeha AH, Ibrahim AA, Abasaeed AE. Ni supported on La_2O_3+ZrO_2 for dry reforming of methane: The impact of surface adsorbed oxygen species. Int J Hydrogen Energy 2021;46:3780–8.

[35]　Long J, Shu S, Wu Q, Yuan Z, Wang T, Xu Y. Selective cyclohexanol production from the renewable lignin derived phenolic chemicals catalyzed by Ni/MgO. Energy Convers Manag 2015;105:570–7.

[36]　Teterycz H, Klimkiewicz R, Łaniecki M. The role of Lewis acidic centers in stabilized zirconium dioxide. Appl Catal A Gen 2003;249:313–26.

[37]　Centi G, Cerrato G, D'Angelo S, Finardi U, Giamello E, Morterra C. Catalytic behavior and nature of active sites in copper-on-zirconia catalysts for the decomposition of N_2O. Catal Today 1996;27:265–70.

[38]　Jakobsen JG, Jørgensen TL, Chorkendorff I, Sehested J. Steam and CO_2 reforming of methane over a Ru/ZrO_2 catalyst. Appl Catal A Gen 2010;377:158–66.

[39]　Yamaguchi T. Application of ZrO_2 as a catalyst and a catalyst support. Catal Today 1994;20:199–217.

[40]　Saha B, Khan A, Ibrahim H, Idem R. Evaluating the performance of non-precious metal based catalysts for sulfur-tolerance during the dry reforming of biogas. Fuel 2014;120:202–17.

[41]　Al-Doghachi FAJ, Taufiq-Yap YH. CO_2 Reforming of Methane over Ni/MgO Catalysts Promoted with Zr and La Oxides. ChemistrySelect 2018;3:816–27.

[42]　Al-Fatesh ASA, Fakeeha AH. Effects of calcination and activation temperature on dry reforming catalysts. J Saudi Chem Soc 2012;16:55–61.

[43]　Donohue MD, Aranovich GL. Classification of Gibbs adsorption isotherms. Adv Colloid Interface Sci 1998;76–77:137–52.

[44]　Yang X, Wang Y, Wang Y. Significantly Improved Catalytic Performance of Ni-Based MgO Catalyst in Steam Reforming of Phenol by Inducing Mesostructure. Catal 2015;5.

25

[45]　Horváth A, Németh M, Beck A, Maróti B, Sáfrán G, Pantaleo G. Strong impact of indium promoter on Ni/Al$_2$O$_3$ and Ni/CeO$_2$-Al$_2$O$_3$ catalysts used in dry reforming of methane. Appl Catal A Gen 2021;621:118174.

[46]　Mesrar F, Kacimi M, Liotta LF, Puleo F, Ziyad M. Syngas production from dry reforming of methane over ni/perlite catalysts: Effect of zirconia and ceria impregnation. Int J Hydrogen Energy 2018;43:17142–55.

[47]　Eltejaei H, Reza Bozorgzadeh H, Towfighi J, Reza Omidkhah M, Rezaei M, Zanganeh R. Methane dry reforming on Ni/Ce$_{0.75}$Zr$_{0.25}$O$_2$-MgAl$_2$O$_4$ and Ni/Ce$_{0.75}$Zr$_{0.25}$O$_2$-γ-alumina: Effects of support composition and water addition. Int J Hydrogen Energy 2012;37:4107–18.

[48]　Ding M, Tu J, Zhang Q, Wang M, Tsubaki N, Wang T. Enhancement of methanation of bio-syngas over CeO$_2$-modified Ni/Al$_2$O$_3$ catalysts. Biomass and Bioenergy 2016;85:12–7.

[49]　Dębek R, Motak M, Duraczyska D, Launay F, Galvez ME, Grzybek T. Methane dry reforming over hydrotalcite-derived Ni-Mg-Al mixed oxides: The influence of Ni content on catalytic activity, selectivity and stability. Catal Sci Technol 2016;6:6705–15.

[50]　Jeong MG, Kim SY, Kim DH, Han SW, Kim IH, Lee M. High-performing and durable MgO/Ni catalysts via atomic layer deposition for CO2 reforming of methane (CRM). Appl Catal A Gen 2016;515:45–50.

[51]　Daroughegi R, Meshkani F, Rezaei M. Enhanced low-temperature activity of CO$_2$ methanation over ceria-promoted Ni-Al$_2$O3 nanocatalyst. Chem Eng Sci 2021;230:116194.

[52]　He D, Luo Y, Tao Y, Strezov V, Nelson P, Jiang Y. Promoter Effects on Nickel-Supported Magnesium Oxide Catalysts for the Carbon Dioxide Reforming of Methane. Energy & Fuels 2017;31:2353–9.

[53]　Olah GA, Goeppert A, Czaun M, Prakash GKS. Bi-reforming of Methane from Any Source with Steam and Carbon Dioxide Exclusively to Metgas (CO–2H$_2$) for Methanol and Hydrocarbon Synthesis. J Am Chem Soc 2013;135:648–50.

[54]　Roh H-S, Koo K, Joshi U, Yoon W. Combined H$_2$O and CO$_2$ reforming of methane over Ni-Ce-ZrO$_2$ catalysts for gas to liquids (GTL). Catal Letters 2008;125:283–8.

[55]　Koo KY, Roh HS, Jung UH, Seo DJ, Seo YS, Yoon WL. Combined H$_2$O and CO$_2$ reforming of CH4 over nano-sized Ni/MgO-Al$_2$O$_3$ catalysts for synthesis gas production for gas to liquid (GTL): Effect of Mg/Al mixed ratio on coke formation. Catal Today 2009;146:166–71.

[56]　Itkulova SS, Nurmakanov YY, Kussanova SK, Boleubayev YA. Production of a hydrogen-enriched syngas by combined CO$_2$-steam reforming of methane over Co-based catalysts supported on alumina modified with zirconia. Catal Today 2018;299:272–9.

[57]　Brush A, Evans EJ, Mullen GM, Jarvis K, Mullins CB. Tunable Syn-gas ratio via bireforming over coke-resistant Ni/Mo$_2$C catalyst. Fuel Process Technol 2016;153:111–20.

[58]　Soria MA, Mateos-Pedrero C, Guerrero-Ruiz A, Rodríguez-Ramos I. Thermodynamic and experimental study of combined dry and steam reforming of methane on Ru/ ZrO$_2$-La$_2$O$_3$ catalyst at low temperature. Int J Hydrogen Energy 2011;36:15212–20.

[59]　Ashok J, Bian Z, Wang Z, Kawi S. Ni-phyllosilicate structure derived Ni-SiO$_2$-MgO catalysts for bi-reforming applications: Acidity, basicity and thermal stability. Catal Sci Technol 2018;8:1730–42.

[60]　Noronha F, Shamsi A, Taylor C, Fendley E, Stagg-Williams S, Resasco D. Catalytic Performance of Pt/ZrO$_2$ and Pt/Ce-ZrO$_2$ Catalysts on CO$_2$ Reforming of CH$_4$ Coupled with Steam Reforming or Under High Pressure. Catal Lett - Catal LETT 2003;90:13–21.

[61]　Yao Y, Gao B, Chen J, Yang L. Engineered Biochar Reclaiming Phosphate from Aqueous

Solutions: Mechanisms and Potential Application as a Slow-Release Fertilizer. Environ Sci Technol 2013;47.

[62]　Pawlak DA, Ito M, Oku M, Shimamura K, Fukuda T. Interpretation of XPS O (1s) in Mixed Oxides Proved on Mixed Perovskite Crystals. J Phys Chem B 2002;106:504–7.

[63]　Lv Z, Zhong Q, Bu Y. In-situ conversion of rGO/Ni2P composite from GO/Ni-MOF precursor with enhanced electrochemical property. Appl Surf Sci 2018;439:413–9.

[64]　Zhang X, Li L, Zhou Q, Liang X, Liu D. Facile synthesis of novel gully-like double-sized mesoporous structural Sr-doped ZrO_2–TiO_2 composites with improved photocatalytic efficiency. J Solid State Chem 2019;269:375–85.

[65]　Rajan AS, Sampath S, Shukla AK. An in situ carbon-grafted alkaline iron electrode for iron-based accumulators. Energy Environ Sci 2014;7:1110–6.

[66]　Al–Fatish ASA, Ibrahim AA, Fakeeha AH, Soliman MA, Siddiqui MRH, Abasaeed AE. Coke formation during CO_2 reforming of CH_4 over alumina-supported nickel catalysts. Appl Catal A Gen 2009;364:150–5.

[67]　Takenaka S, Serizawa M, Otsuka K. Formation of filamentous carbons over supported Fe catalysts through methane decomposition. J Catal 2004;222:520–31.

[68]　He L, Hu S, Jiang L, Syed-Hassan SSA, Wang Y, Xu K. Opposite effects of self-growth amorphous carbon and carbon nanotubes on the reforming of toluene with Ni/α-Al_2O_3 for hydrogen production. Int J Hydrogen Energy 2017;42:14439–48.

27